NASA/CR-2000-210324
ICASE Report No. 2000-32

Closed-loop Separation Control Using Oscillatory Flow Excitation

Brian G. Allan
ICASE, Hampton, Virginia

Jer-Nan Juang and David L. Raney
NASA Langley Research Center, Hampton, Virginia

Avi Seifert
Tel Aviv University, Ramat-Aviv, Israel

Latunia G. Pack and Donald E. Brown
NASA Langley Research Center, Hampton, Virginia

Institute for Computer Applications in Science and Engineering
NASA Langley Research Center, Hampton, VA
Operated by Universities Space Research Association

National Aeronautics and
Space Administration

Langley Research Center
Hampton, Virginia 23681-2199

Prepared for Langley Research Center
under Contract NAS1-97046

August 2000

CLOSED-LOOP SEPARATION CONTROL USING OSCILLATORY FLOW EXCITATION

BRIAN G. ALLAN*, JER-NAN JUANG†, DAVID L. RANEY‡, AVI SEIFERT§, LATUNIA G. PACK¶, AND DONALD E. BROWN‖

Abstract. Design and implementation of a digital feedback controller for a flow control experiment was performed. The experiment was conducted in a cryogenic pressurized wind tunnel on a generic separated configuration at a chord Reynolds number of 16 million and a Mach number of 0.25. The model simulates the upper surface of a 20% thick airfoil at zero angle-of-attack. A moderate favorable pressure gradient, up to 55% of the chord, is followed by a severe adverse pressure gradient which is relaxed towards the trailing edge. The turbulent separation bubble, behind the adverse pressure gradient, is then reduced by introducing oscillatory flow excitation just upstream of the point of flow separation. The degree of reduction in the separation region can be controlled by the amplitude of the oscillatory excitation. A feedback controller was designed to track a given trajectory for the desired degree of flow reattachment and to improve the transient behavior of the flow system. Closed-loop experiments demonstrated that the feedback controller was able to track step input commands and improve the transient behavior of the open-loop response.

Key words. active flow control, experimental, fluid mechanics, separation control, feedback, closed-loop

AMS subject classification. Applied Numerical Mathematics, Controls

1. Introduction. Experiments conducted by Seifert et al. [6, 7, 8] have shown that the introduction of oscillatory flow excitation into a separated flow region can fully reattach the flow or reduce the degree of flow separation. These experiments were performed on various airfoils at low and high Reynolds numbers. They demonstrated that the lift can be significantly enhanced when introducing periodic excitation upstream of the separated flow region. This enhancement is achieved by exciting the flow at frequencies that generate $2-4$ spanwise coherent vortices over the length of the separated region. This periodic excitation increases the momentum transfer across the shear-layer, enhancing its resistance to flow separation due to curvature and adverse pressure gradients. The experiments conducted by Seifert and Pack [8, 9] also demonstrate that there is a range in which the response of the flow is proportional and even linear to the magnitude of the periodic excitation. These flow experiments have been conducted in an open-loop, or man in the loop, fashion. The goal of the present research is to add feedback control to the experimental setup used by Seifert and Pack [8]. This controller will then vary the magnitude of the oscillatory excitation in order to achieve a desired degree of flow attachment characterized by a surface pressure gradient.

2. Experimental Setup. The experiment was conducted in the 0.3-meter Transonic Cryogenic Wind Tunnel at NASA Langley Research Center. This tunnel is a fan driven, closed loop system, with a $0.33\,m$ by $0.33\,m$ test cross section and uses gaseous nitrogen (GN_2) as the test medium. The tunnel operates at stagnation pressures ranging from $1.2\,bar$ up to 6 bar and total temperatures from $78\,K$ up to $327\,K$ [4, 5]. A fully automatic control system maintains

*Institute for Computer Applications in Science and Engineering, Mail Stop 132, NASA Langley Research Center, Hampton, VA 23681-2199 (email: **allan@icase.edu**). This research was supported by the National Aeronautics and Space Administration under NASA Contract No. NAS1-97046 while the author was in residence at the Institute for Computer Applications in Science and Engineering (ICASE), NASA Langley Research Center, Hampton, VA 23681-2199.

†Structural Dynamics Branch, Mail Stop 230, NASA Langley Research Center, Hampton, VA 23681-2199, (email: **j.juang@larc.nasa.gov**)

‡Dynamics and Control Branch, Mail Stop 406, NASA Langley Research Center, Hampton, VA 23681-2199, (email: **d.l.raney@larc.nasa.gov**)

§Department of Fluid Mechanics and Heat Transfer, Faculty of Engineering Tel Aviv University, Ramat-Aviv 69978, Israel, (email: **seifert@eng.tau.ac.il**)

¶Flow Physics and Control Branch, Mail Stop 170, NASA Langley Research Center, Hampton, VA 23681-2199, (email: **l.g.pack@larc.nasa.gov**)

‖Lockheed Martin, Mail Stop 463, NASA Langley Research Center, Hampton, VA 23681-2199, (email: **d.e.brown@larc.nasa.gov**)

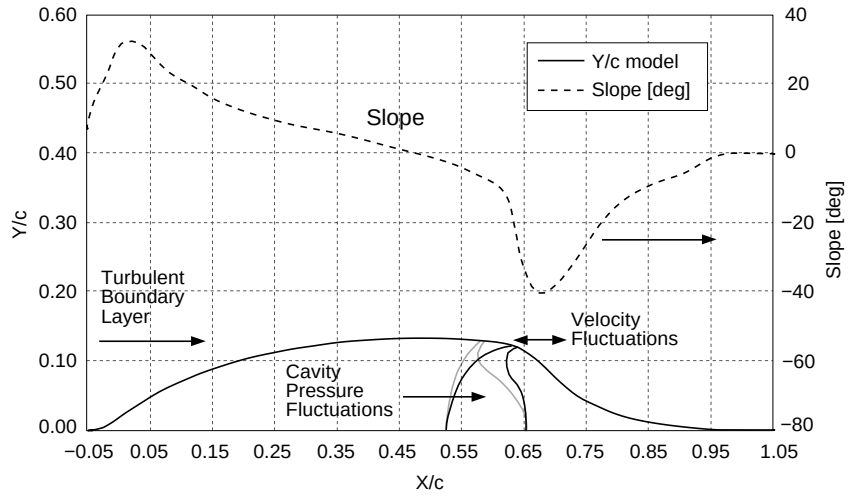

FIG. 2.1. *Hump configuration.*

the test conditions, providing a high level of repeatability.

2.1. Hump Model. The test model simulates the upper surface of a 20% thick airfoil that is a variation on the Glauert Glas II airfoil [8]. The model contour generates a mild favorable pressure gradient until $x/c = 0.55$. This is followed by a severe adverse pressure gradient that is relaxed towards the trailing edge as shown in Fig. 2.1. Without control, the flow separates at the slope discontinuity, $x/c \approx 0.66$. Two alternative blowing slot locations are available: $x/c = 0.59$ and 0.64 (both shown on Fig. 2.1). The position of the upstream slot was selected so it would be upstream of the expected position of a shock wave. All of the experiments conducted in this investigation used the downstream slot at $x/c = 0.64$. The slots were about 0.25% chord wide ($0.50\,mm \pm 20\%$), and allowed an almost tangential downstream introduction of momentum (the slots are inclined at 30^o to the surface because of manufacturing considerations, see Fig. 2.1).

2.2. Oscillatory Blowing Valve. A rotating, siren type, valve was used to generate pressure oscillations inside the model cavity. The oscillatory blowing valve was capable of generating frequencies up to $800\,Hz$, and for safety reasons was rated to $300\,psi$. GN_2 was supplied to the valve by converting a portion of the liquid nitrogen (LN_2) available for operating the tunnel using an ambient temperature vaporizer. The use of ambient temperature GN_2 simplified the valve design. A pressure regulator was used to control the GN_2 entering the valve and the variable speed drive of the valve motor was used to control the frequency of the pressure oscillations. The oscillatory blowing valve was attached to the right tunnel plenum door at the center of rotation of the turntable (Fig. 2.2). The outlet of the oscillatory blowing valve was connected to the backside of the model cavity. The $76.2\,mm$ inner diameter pipe, exiting the oscillatory blowing valve, was converted to a rectangular cross section and then split into five square diverging ducts that fit into the $330\,mm$ by $25.4\,mm$ entrance to the model cavity. Seven suction ports were positioned between and around the five square ducts at the exit of the manifold. These ports were connected to the left side tunnel boundary-layer removal system. The digital valves of the left side boundary-layer removal system were used to control the steady flow rate out of the manifold shown in Fig 2.2. This flow is driven by the tunnel static pressure which is higher than the ambient pressure. Any relevant combination of steady and oscillatory excitation could be generated with this type of control. Steady suction or steady blowing could be applied in a similar manner by holding the oscillatory blowing valve in the fully open position and varying the inlet or the exhaust mass flow rates.

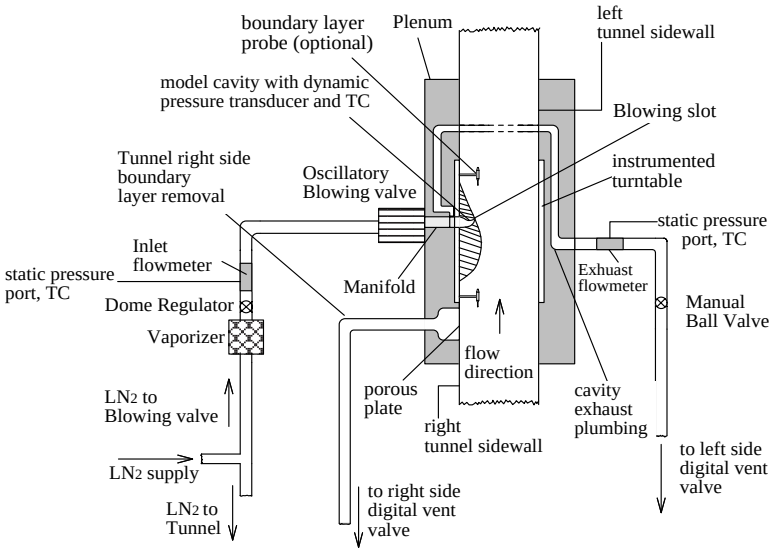

FIG. 2.2. *Experimental setup.*

2.3. Instrumentation. The model surface pressures were measured at 60 locations by the facility data acquisition system. Normal force, moment, and form-drag were calculated from these measurements. Turbine flow meters on the inlet of the oscillatory blowing valve and on the exhaust side of the model cavity (through the manifold) were used to measure the flow volume entering and exiting the model cavity. The volume flow rate measurements were combined with temperature and pressure measurements to determine the mass flux entering and exiting the model cavity (see Fig. 2.2). The steady mass flux in or out of the slot could be determined by subtracting the two mass fluxes. A dynamic pressure transducer, flush-mounted in the model cavity, was used to measure the pressure fluctuations produced by the oscillatory blowing valve. A Thermocouple was installed inside the cavity to allow (using also the tunnel static pressure) calculation of the GN_2 density in the cavity. The normalized cavity pressure fluctuation, ρ'/ρ_∞, were shown to be directly related to the excitation unsteady momentum, $<c_\mu>$, that is the leading control authority of the periodic excitation when using optimal frequencies [9].

2.4. Closed-Loop System. The block diagram in Fig. 2.3 represents the setup of the experimental closed-loop system in the laboratory. This diagram shows the interconnection between the PC, actuator, and sensors. The amplitude of the control jet can be modulated using the PC which sends an IEEE pressure command, P_i, to the mensor unit. The mensor unit then outputs a pressure equal to P_i, to the dome pressure regulator, which supplies the GN_2 to the oscillatory blowing valve. Figure 2.3 shows how the digital exhaust valve is controlled by the PC which sends a second IEEE command, $\dot{m}_{ec}$, to the digital exhaust valve. This IEEE command is received by a unit which will open and close a desired combination of solenoid valves equalizing the mass flow rate entering and exiting the cavity of the model.

The pressure gradient, dC_P/dx, was measured using a differential pressure transducer. This sensor measured the pressure difference between stations, $x/c = 0.952$ and 0.489. This pressure gradient is used to characterize the degree of flow reattachment on the hump model and will be referred to as the pressure recovery parameter. The output voltage from the transducers are sent to a low pass filter, amplified, and then sampled by the DSP board on the PC. The signal from the dynamic pressure sensor, inside the cavity of the hump model, is passed through a RMS to DC converter and then amplified before being sampled by the DSP board. The DSP board samples these two signals at a rate of $100\,Hz$. This data can either be uploaded as raw sampled data to the PC or averaged over a desired length of time and then uploaded to the PC. In the closed-loop experiments conducted here, the sampled data was averaged over a $0.5\,s$

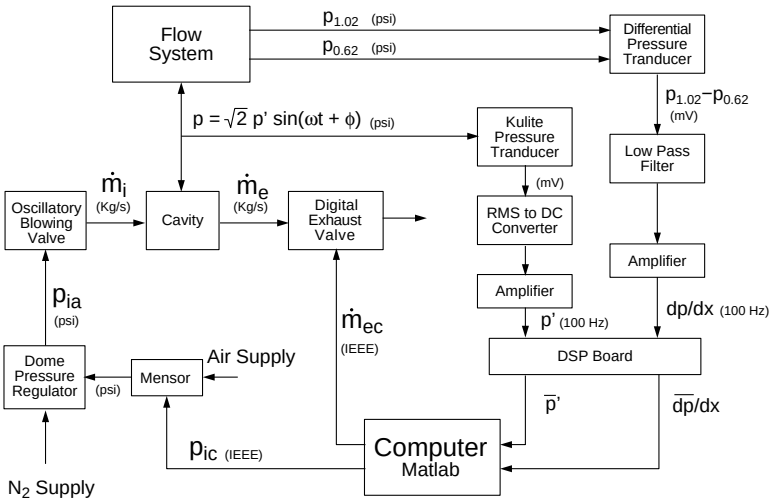

FIG. 2.3. *Block diagram of experimental system.*

interval and then uploaded at every second from the DSP board to the PC.

3. System Model. A linear system model was developed for the feedback control design process. The actual system has some nonlinear effects which are neglected in the linear system model but will be incorporated in a nonlinear model. The nonlinear model will be used to evaluate the feedback controller developed from the linear system model.

3.1. Continuous System Model. The dynamics of the flow system were modeled by lumping the system components into two separate systems as shown in Fig. 3.1. The first system models the dynamic response from the IEEE command, $P_i - P_s$, to the RMS pressure fluctuations in the cavity, p'/ρ_∞. This system will represent the dynamics of the actuator system. The second system represents the dynamic response of the flow system and models the response of the pressure recovery parameter, dC_P/dx, to the cavity RMS pressure fluctuations, p'/ρ_∞. Both systems are modeled using a simple second-order damped system. The second-order model was chosen since the dynamics of the experimental system are unknown and the dynamics of most mechanical systems can be approximated by this type of general model. If the second-order model is determined to be insufficient a model of increased complexity can be used.

The dynamics of the actuator system are modeled by the simple second-order system

$$\frac{d^2}{dt^2}\left[\frac{p'(t)}{\rho_\infty}\right] = -2\zeta_1\omega_{n1}\frac{d}{dt}\left[\frac{p'(t)}{\rho_\infty}\right] - \omega_{n1}^2\left[\frac{p'(t)}{\rho_\infty}\right] + \omega_{n1}^2\left[m_1(P_i - P_s) - b_1\right] \tag{3.1}$$

where ζ_1 is the damping ratio and ω_{n1} the natural undamped frequency. The constants m_1 and b_1 are the slope and intercept of the linear fit to the steady-state data of p'/ρ_∞ as a function of $P_i - P_s$. The steady-state relation $(p'/\rho_\infty)_{ss} = f([P_i - P_s]_{ss})$, is then approximated by the linear fit

$$\left(\frac{p'}{\rho_\infty}\right)_{ss} = m_1(P_i - P_s)_{ss} + b_1 \tag{3.2}$$

where $(p'/\rho_\infty)_{ss}$ and $(P_i - P_s)_{ss}$ are the steady-state values of (p'/ρ_∞) and $(P_i - P_s)$ respectively. Similarly, the dynamic response of the pressure recovery parameter, dC_P/dx, to the cavity pressure fluctuations, $p'(t)/\rho_\infty$, is modeled by the second-order system

$$\frac{d^2}{dt^2}\left[\frac{dC_P(t)}{dx}\right] = -2\zeta_2\omega_{n2}\frac{d}{dt}\left[\frac{dC_P(t)}{dx}\right] - \omega_{n2}^2\left[\frac{dC_P(t)}{dx}\right] + \omega_{n2}^2\left[m_2\frac{p'(t)}{\rho_\infty} - b_2\right] \tag{3.3}$$

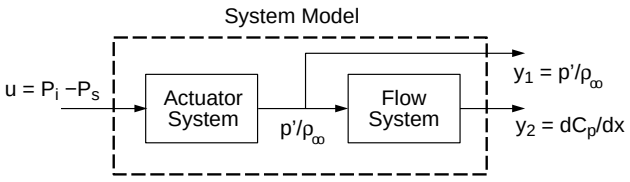

FIG. 3.1. *Two system model*

The constants m_2 and b_2 are the slope and intercept of the linear fit to the steady-state data for dC_P/dx as a function of p'/ρ_∞. The steady-state function $(C_P)_{ss} = g([p'/\rho_\infty]_{ss})$ is then approximated by the linear fit

$$(dC_P/dx)_{ss} = m_2(p'/\rho_\infty)_{ss} + b_2 \tag{3.4}$$

Next, define the state vector $\mathbf{x} = [x_1, x_2, x_3, x_4]^T = [p'/\rho_\infty,\ d/dt(p'/\rho_\infty),\ dC_P/dx,\ d/dt(dC_P/dx)]^T$. Using this state vector, Eq. 3.1 and Eq. 3.3 can be expressed as

$$\frac{d}{dt}\begin{bmatrix} x_1 \\ x_2 \\ x_3 \\ x_4 \end{bmatrix} = \begin{bmatrix} 0 & 1 & 0 & 0 \\ -\omega_{n1}^2 & -2\zeta_1\omega_{n1} & 0 & 0 \\ 0 & 0 & 0 & 1 \\ 0 & 0 & -\omega_{n2}^2 & -2\zeta_2\omega_{n2} \end{bmatrix}\begin{bmatrix} x_1 \\ x_2 \\ x_3 \\ x_4 \end{bmatrix} + \begin{bmatrix} 0 & 0 \\ \omega_{n1}^2 m_1 & 0 \\ 0 & 0 \\ 0 & \omega_{n2}^2 m_2 \end{bmatrix}\begin{bmatrix} P_i - P_s \\ p'/\rho_\infty \end{bmatrix} + \begin{bmatrix} 0 \\ -\omega_{n1}^2 b_1 \\ 0 \\ -\omega_{n2}^2 b_2 \end{bmatrix} \tag{3.5}$$

Substituting $p'/\rho_\infty = x_1$ for the input term results in

$$\dot{\mathbf{x}} = \underbrace{\begin{bmatrix} 0 & 1 & 0 & 0 \\ -\omega_{n1}^2 & -2\zeta_1\omega_{n1} & 0 & 0 \\ 0 & 0 & 0 & 1 \\ \omega_{n2}^2 m_2 & 0 & -\omega_{n2}^2 & -2\zeta_2\omega_{n2} \end{bmatrix}}_{A}\mathbf{x} + \underbrace{\begin{bmatrix} 0 \\ \omega_{n1}^2 m_1 \\ 0 \\ 0 \end{bmatrix}}_{B}(P_i - P_s) + \underbrace{\begin{bmatrix} 0 \\ -\omega_{n1}^2 b_1 \\ 0 \\ -\omega_{n2}^2 b_2 \end{bmatrix}}_{\mathbf{f}} \tag{3.6}$$

Defining $u = P_i - P_s$, the equation above can be expressed in the matrix form

$$\dot{\mathbf{x}} = A\mathbf{x} + Bu + \mathbf{f} \tag{3.7}$$

where the vector $\mathbf{f}$ is a drift (or bias) term. The output vector $\mathbf{y} = [y_1, y_2]^T$ is defined as

$$\mathbf{y} = \begin{bmatrix} p'/\rho_\infty \\ dC_p/dx \end{bmatrix} = \begin{bmatrix} 1 & 0 & 0 & 0 \\ 0 & 0 & 1 & 0 \end{bmatrix}\mathbf{x} = C\mathbf{x} \tag{3.8}$$

The drift term $\mathbf{f}$ can be removed by considering the steady-state solution to Eq. 3.7

$$0 = A\mathbf{x}_{ss} + Bu_{ss} + \mathbf{f} \tag{3.9}$$

where u_{ss} and $\mathbf{x}_{ss}$ are the steady-state input and state vectors respectively. A new state variable $\hat{\mathbf{x}}$ is now defined as

$$\hat{\mathbf{x}} = \mathbf{x} - \mathbf{x}_{ss} \tag{3.10}$$

Substituting this relation into Eq. 3.7 and using Eq. 3.9 results in

$$\dot{\hat{\mathbf{x}}} = A\hat{\mathbf{x}} + Bv \tag{3.11}$$

FIG. 3.2. *Simplified block model*

where $v = u - u_{ss}$. Using the definition of $\hat{\mathbf{x}}$, the output equation for $\mathbf{y}$ becomes

$$\begin{aligned} \mathbf{y} &= C\hat{\mathbf{x}} + C\mathbf{x}_{ss} \\ &= \hat{\mathbf{y}} + C\mathbf{x}_{ss} \end{aligned} \tag{3.12}$$

where $\hat{\mathbf{y}} = C\hat{\mathbf{x}}$. The new system without the drift term can be summarized as

$$\begin{aligned} \dot{\hat{\mathbf{x}}} &= A\hat{\mathbf{x}} + Bv \\ \hat{\mathbf{y}} &= C\hat{\mathbf{x}} \end{aligned} \tag{3.13}$$

where

$$\begin{aligned} \mathbf{x} &= \hat{\mathbf{x}} + \mathbf{x}_{ss} \\ \mathbf{y} &= \hat{\mathbf{y}} + C\mathbf{x}_{ss} \\ u &= v + u_{ss} \end{aligned} \tag{3.14}$$

The system in Eq. 3.13 is expressed as the simplified block, P, shown in Fig. 3.2 where P has one input v and two outputs $\hat{y}_1$ and $\hat{y}_2$. This linear system without the drift term can now be used in the feedback control design.

3.2. Discrete System Model. Sampling of the analog voltages from the pressure transducers was done digitally, making our control system discrete. In order to account for the discrete sampling in our controller, a discrete control design was performed. To design our controller in the discrete domain, the continuous system given in Eq. 3.13 was converted to a discrete system using a zero-order hold.

$$\begin{aligned} \hat{\mathbf{x}}_\mathbf{d}(k+1) &= A_d\hat{\mathbf{x}}_\mathbf{d}(k) + B_d\mathbf{v}_\mathbf{d}(k) \\ \hat{\mathbf{y}}_\mathbf{d}(k) &= C_d\hat{\mathbf{x}}_\mathbf{d}(k) \end{aligned} \tag{3.15}$$

The discrete state variable is defined as, $\hat{\mathbf{x}}_\mathbf{d}(k) = \hat{\mathbf{x}}(kT)$, where T is the sampling period. Using a zero-order hold on the input, the matrices A_d and B_d are given by

$$\begin{aligned} A_d &= e^{AT} \\ B_d &= (A_d - I)A^{-1}B \end{aligned} \tag{3.16}$$

where $C_d = C$ and A is assumed invertible [3].

The parameters for the A and B matrices were determined using steady-state and dynamic open-loop experimental data. The experimental data used to determine the steady-state parameters are shown in Figs. 3.3 and 3.4. Figure 3.3 shows the experimental data for the steady-state relationship between the IEEE command P_i, minus the static wind tunnel pressure P_s, to the cavity pressure fluctuations p' divided by the free stream density ρ_∞. This figure shows that the linear fit represents the experimental data reasonably well, for $P_i - P_s$ above 5. Below $P_i - P_s = 5$, the cavity pressure fluctuations do not respond to the low P_i input. Notice that some of the experimental data points do not fall on the linear fit. This will result in steady-state errors in our linear model near these points. Fig. 3.4 shows the experimental data for the steady-state relation between the cavity pressure fluctuations and the pressure recovery parameter, dC_P/dx.

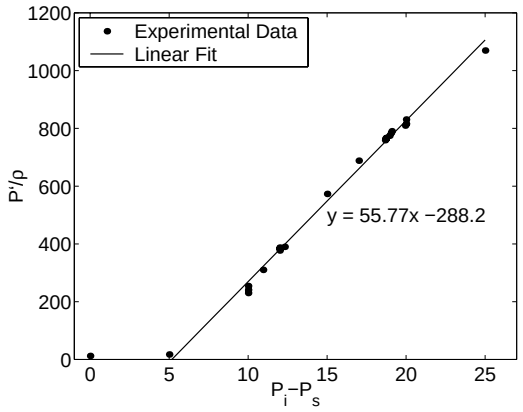

FIG. 3.3. *Steady-state effect of $P_i - P_s$ on p'/ρ_∞.*

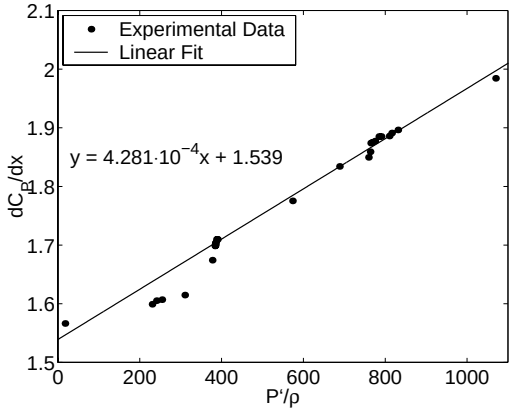

FIG. 3.4. *Steady-state effect of p'/ρ_∞ on dC_P/dx.*

TABLE 3.1
Dynamic parameters for system model.

m_1	55.77	m_2	$4.956 \cdot 10^{-4}$
b_1	-288.2	b_2	1.781
ω_{n1}	0.5000	ω_{n2}	80.00
η_1	0.3400	η_2	1.000

This figure shows a change in the gain for values of $p'/\rho_\infty < 400$. The linear fit is made to the data above $p'/\rho_\infty = 400$ as the controller will typically be operating at cavity pressures fluctuations in this range. The steady-state gains for the linear system are given by the parameters m_1, b_1, m_2, and b_2 shown in Table 3.1.

Figure 3.5 shows the hump model pressure distribution with and without control. The baseline pressure distribution, given by the $P_i - P_s = 0$ line, shows a large separation bubble downstream of the slot. For the baseline pressure distribution, the pressure recovery parameter, dC_P/dx, is equal to 0.77. Applying periodic excitation ($P_i - P_s > 0$) decreases the size of the separation bubble, as shown by the pressure distribution in Fig. 3.5. The $P_i - P_s = 10$ line shows an increase in the pressure recovery parameter, dC_P/dx, of 1.6, as compared to 0.77 given by the baseline pressure distribution. Increasing $P_i - P_s$ to 20, produces a dC_P/dx value of 1.85, indicating a further size reduction of the separation bubble.

Figures 3.6 through 3.9 show the open-loop responses of the experimental system to four different $P_i - P_s$ step input commands. These open-loop responses were used to determine the dynamic parameters in Table 3.1 so that the linear model response would match the experimental results. By changing the values of ω_{n1}, ζ_1, ω_{n2}, and ζ_2 the dynamic characteristics of the linear system model could be fitted to the data. The open-loop experimental data showed that the actuator system was much slower than the response of the flow system. The frequency response of the flow was fixed at $\omega_{n2} = 80$ with a damping ratio of $\zeta_2 = 1$. The parameters ω_{n1} and ζ_1 were then adjusted to fit the experimental data. The oscillations in the experimental data for dC_P/dx were not modeled by the linear model. These small oscillations are believed to be produced by small fluctuations in the wind tunnel test conditions.

Figure 3.6 shows a comparison of the experimental data to the linear model response to a step input from $P_i - P_s =$ 10 to 15. Here the linear model over predicts the initial steady-state cavity pressure fluctuations and pressure recovery parameter for $P_i - P_s = 10$ and under predicts the cavity pressure fluctuations at the final steady-state at $P_i - P_s = 15$. This steady-state offset is a result of the linear fit to the steady-state data. Figure 3.6 does show a good fit to the dynamic response of the experimental system for the cavity pressure fluctuations. The comparison for the pressure

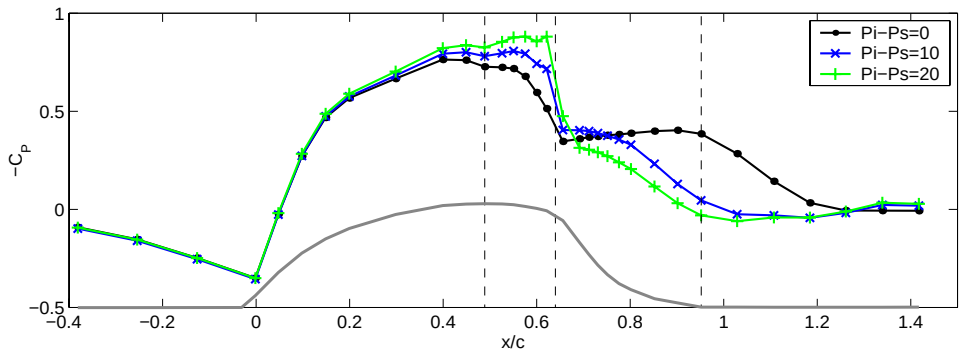

FIG. 3.5. *Steady-state surface pressure profiles for* $P_i - P_s = 0, 5, 10, and 20$

recovery parameter shows good agreement for the transient and the mean steady-state values. Figure 3.7 shows a good prediction of the open-loop dynamics but under predicts the cavity pressure fluctuations. This under prediction by the model is again due to the linear fit of the steady-state experimental data. Figure 3.3 shows that the two experimental points at $P_i - P_s = 15$ and 17 are slightly higher than the linear fit. This difference then shows up in the open-loop simulations as an offset. Figure 3.8 shows a slight over prediction of the steady-state pressure recovery parameter but does capture the dynamics of the step input. Figure 3.9 shows that the model has an offset in both the cavity pressure fluctuations and pressure recovery parameter. This offset is due to an error in the steady-state prediction as can be seen in the linear fit to the steady-state data in Figs. 3.3 and 3.4 for $P_i - P_s = 25$. Overall the linear model does a fair job of predicting the dynamic response of the experimental system and has a slight offset in the steady-state gains of the system.

Using the parameters in Table 3.1 the matrices A and B, for the continuous system in Eq. 3.6, are given as

$$A = \begin{bmatrix} 0 & 1.0 & 0 & 0 \\ -0.25 & -0.34 & 0 & 0 \\ 0 & 0 & 0 & 1 \\ 1.798 & 0 & -6400 & -160 \end{bmatrix} \quad B = \begin{bmatrix} 0 \\ 13.943 \\ 0 \\ 0 \end{bmatrix} \tag{3.17}$$

Using a sample period of $T = 1.0s$, the matrices A_d and B_d for the discrete system, using Eq. 3.15, are

$$A_d = \begin{bmatrix} 0.89030 & 0.81292 & 0 & 0 \\ -0.20323 & 0.61391 & 0 & 0 \\ 2.5158 \cdot 10^{-4} & 2.2401 \cdot 10^{-4} & 0 & 0 \\ -5.6003 \cdot 10^{-5} & 1.7536 \cdot 10^{-4} & 0 & 0 \end{bmatrix} \quad B_d = \begin{bmatrix} 6.1180 \\ 11.334 \\ 1.6407 \cdot 10^{-3} \\ 3.1240 \cdot 10^{-3} \end{bmatrix} \tag{3.18}$$

Note that since the sampling frequency is much lower than the frequency of the flow system, the A_d matrix results in the last two columns being zero. Since the sampling frequency is so low these states could be excluded but been included for completeness. Future actuators will have an improved response in the high frequency range where the inclusion of the flow dynamics will be necessary.

4. Feedback Control Design. A feedback controller was designed for this system using a simple proportional-integral-derivative (PID) controller. The advantage of using a PID controller is that it can be tuned to give good performance results where only the dominate system time constants are known [2].

Figure 4.1 shows a block diagram of a basic PID feedback controller for a continuous closed-loop system. This figure shows the output, $y(t)$, being subtracted from the desired output, $y_{des}(t)$, to produce an error signal, $e(t)$. Given

the error signal, $e(t)$, the input, $u(t)$, can be computed by

$$u(t) = K_P e(t) + K_I \int_0^t e(t)dt + K_D \frac{de(t)}{dt} \tag{4.1}$$

The constant K_P can be adjusted to vary the amount of proportional feedback for the controller. Likewise, the constants K_I and K_D are used to vary the degree of integral gain and derivative gain respectively.

Increasing the proportional gain will typically reduce the steady-state error and settling time of the closed-loop system. However, large K_P values usually produces instability in the closed-loop system. For most systems, there is an upper limit on the gain K_P in order to achieve a well-damped, stable response. This upper limit on K_P may still result in unacceptable steady-state errors, putting a limit on how much the steady-state errors can be reduced using proportional feedback alone.

To improve the steady-state accuracy, without needing a large proportional gain, integral control can be used. Integral control will reduce or eliminate steady-state errors at the cost of reduced transient response performance. When the steady-state error is small, the proportional gain times the error will produce a small control input, assuming that the proportional gain can not be arbitrarily large. This small input from proportional feedback alone, will typically be too small to change the steady-state error. Integral gain on the other hand, will integrate the small error over time, producing an increasing control input until the system responds. This input from the integral gain will eventually reduce or eliminate the steady-state error. Like the proportional gain, the integral gain, K_I, also has an upper limit in order to achieve a well-damped, stable response.

Derivative control can be added to increase the damping and increase the stability of the closed-loop system. Since the derivative of the error represents the slope of the error, $e(t)$, the derivative feedback is essentially an anticipatory type of control. Normally, if the slope of the error is large, an overshoot will subsequently occur. The derivative control can be used to predict an overshoot by measuring the slope of the error and making a proper correcting effort before the overshoot actually occurs.

4.1. Discrete PID Controller. The PID controller was implemented using a computer which resulted in the need for a digital controller. To account for the discrete nature of the digital controller in the control design, the controller was designed in the discrete domain.

Approximation of the continuous integral controller was done using a trapezoidal method. Let $g_I(kT)$ be the numerical approximation to the integral of the error at $t = kT$, where $g_I(0) = 0$. Using the trapezoidal method, $g_I(kT)$ can be written as

$$g_I(kT) = g_I[(k-1)T] + \frac{T}{2}[e(kT) + e((k-1)T)] \tag{4.2}$$

Taking the z-transform on both sides of Eq. 4.2 results in the transfer function

$$M_I(z) = \frac{G_I(z)}{E(z)} = \frac{T(z+1)}{2(z-1)} \tag{4.3}$$

where $M_I(z)$ is a discrete transfer function from the error to the integral of error. The discrete approximation to the derivative was made using a backward difference method. Let $g_D(kT)$ be the approximation to the derivative of the error at $t = kT$ resulting in

$$g_D(kT) = \frac{1}{T}\{e(kT) - e[(k-1)T]\} \tag{4.4}$$

Taking the z-transform on both sides of Eq. 4.4 results in the transfer function

$$M_D(z) = \frac{G_D(z)}{E(z)} = \frac{z-1}{Tz} \tag{4.5}$$

where $M_D(z)$ is a discrete transfer function from the error, to the derivative of the error. Combining the proportional, integral, and derivative controllers, results in the transfer function from the error, $E(z)$, to the control input $U(z)$ becomes

$$H(z) = \frac{U(z)}{E(z)} = K_P + K_I M_I(z) + K_D M_D(z) \tag{4.6}$$

where $H(z)$ is the discrete transfer function for the PID controller from the error signal to the control input. Substituting Eq. 4.3 and 4.5 and simplifying results in

$$H(z) = \frac{\left(K_P + \frac{TK_I}{2} + \frac{K_D}{T}\right) z^2 + \left(-K_P + \frac{TK_I}{2} - \frac{2K_D}{T}\right) z + \frac{K_D}{T}}{z(z-1)} \tag{4.7}$$

Figure 4.2 shows a block diagram of the transfer function in Eq. 4.7.

4.2. Discrete PID Control Design. The block diagram in Fig. 4.3 shows the closed-loop system with the discrete PID controller, $H(z)$, and the linear system model, $P(z)$. The closed-loop system also includes an external disturbance, *w*, which can be used to model the effects of the pressure oscillations created by small fluctuations in the wind tunnel test conditions. The effects of these fluctuations can be seen in the open-loop experimental data in Figs. 3.6 through 3.9. The objectives of the control design is to track a desired dC_P/dx command while minimizing the overshoot. Since the actuators for this system were fairly slow, minimizing the effects of wind tunnel fluctuations was not possible and therefore not a control objective. The response time of the controller was considered a secondary objective and was relaxed in favor of smoother transient behavior.

Figure 4.4 shows a root locus plot in the z-plane for the poles of the discrete closed-loop system. The plot also shows the lines of constant damping, ζ, and natural frequency, ω_n, transformed from the s-plane to the z-plane. Poles inside of the unit circle, in the z-pane, are stable and poles outside are unstable. The open-loop system has four poles which are shown in Fig. 4.4 as open circles. The two high frequency poles in the s-plane are mapped to the origin, since the sample frequency is well below the frequency of these poles. Increasing K_P while holding $K_I = K_D = 0$, moves the two low frequency open-loop poles to a higher natural frequency, while decreasing the damping ratio. The closed-loop poles cross the unit circle at $K_P = 117$ where larger values of K_P result in an unstable closed-loop system. Increasing the integral gain, K_I, while holding $K_P = K_D = 0$, also moves the low frequency poles towards the unit circle. At $K_I = 12.7$, the poles cross the unit circle where larger values of K_I make the closed-loop system unstable. The integral controller also introduces a fifth pole which moves along the real axis, from one to zero, as K_I increases.

The time response of the closed-loop system, for increasing values of K_P and K_I, are shown in Figs. 4.5 through 4.8. The figures show the response of the closed-loop system, where the controller is turned on at $t = 0$ with a desired $dC_P/dx = 1.8$. Figures 4.5 and 4.6 show how using only proportional gain results in a significant steady-state error. This error is a result of the constant control input needed in order for the system to reach the desired steady-state point. Since the proportional gain is a product of the error, the error could never go to zero while generating the constant control signal needed for the new steady-state point. By increasing the gain K_P, the error is reduced only slightly at the cost of reduced damping. This reduced damping effect can be explained by the root locus plot in Fig. 4.4 where the closed-loop pole is moved closer to the unit circle as K_P is increased. Figures 4.7 and 4.8 show the effect of only using an integral controller for a step input command. These figures show how the integral controller dramatically reduces the steady-state error as compared to the K_D gain. Unlike the proportional gain, the integral gain is able to generate a constant input signal in order to reach the new steady-state point. By increasing K_I, the response time decreases but at the cost of decreased damping. Like the proportional controller, increasing K_I moves the two poles toward the unit circle decreasing the damping for these poles.

To improve the damping of the closed-loop system for high gains, derivative feedback gain can be added. However this gain can cause problems when there is significant noise in the system as is the case here. The noise in the system was shown in the open-loop experimental data in Figs. 3.6 through 3.9. As a result of the noise content in our system, the derivative feedback gain was not used. However if minimizing the response time was the main control objective then derivative feedback might be needed.

To see how the K_P and K_I gains are effected by the wind tunnel fluctuations, a Bode plot for the transfer function between the disturbance input, w, and error, e, are plotted in Figs. 4.9 and 4.10. Figure 4.9 shows how increasing the K_I amplifies noise signals in the 0.03 to $0.1\,Hz$ range and remains fairly flat above $0.1\,Hz$. This is good since the large amplitude oscillations due to the wind tunnel noise fall in the 0.17 to $0.12\,Hz$ range. Figure 4.10 shows that increasing K_P will increase the error signal for noise in the 0.08 to $0.3\,Hz$ range. This means that using a proportional gain will amplify the oscillations produced by the fluctuations in the wind tunnel test conditions. Therefore in order not to amplify these oscillations, proportional gain was not used.

5. Nonlinear Simulation. A nonlinear model of the experimental system was developed using the SIMULINK toolbox which operates in the MATLAB computing environment [1]. This model includes the nonlinear effects of the steady-state gains as shown in Figs. 3.3 and 3.4, as well as the limiters applied to the control input. This simulation also accounted for the discrete time sampling and averaging of the pressure sensor signals by the DSP board. Figure 5.1 shows the main block diagram of the experimental system which simulates the closed-loop step response of dC_P/dx to a step input command in the desired dC_P/dx value. This simulation model was used to evaluate the feedback controller after it was designed using the linear system model.

The discrete PID controller is shown as a single block in Fig. 5.1 with two inputs and one output. The contents of this subblock are shown in Fig. 5.2 where the two inputs are subtracted to make an error signal which is then passed to the proportional, integral, and derivative gains. These gains are summed up to make the control output signal $P_i - P_s$. The $P_i - P_s$ signal is then passed through the discrete rate and saturation limiters shown in Fig. 5.3. These limiters were used to keep the flow system in a safe operating range. The output from the limiters is then sent to the flow system model shown in Fig. 5.4. This system models the nonlinear response of the actuator from the input signal $P_i - P_s$, to the output signal dC_P/dx. A lookup table was used for the nonlinear steady-state gains and the dynamics of the system were modeled using the second-order system described in section 3.

The closed-loop model shown in Fig. 5.1 uses the sensor measurement of the pressure recovery parameter, dC_P/dx, which is sampled by the DSP board. The DSP board samples voltage of the differential pressure transducer at a frequency of $100\,Hz$. This signal is sampled and averaged over a time period of $0.5\,s$. The averaged signal is then sent to the discrete controller at a rate of $1\,Hz$. The averaging procedure is modeled by the averaging block in Fig. 5.1, which is shown in detail in Fig. 5.5. The system in Fig. 5.5 starts summing up the $100\,Hz$ sampled data when given a trigger command. The trigger in Fig. 5.1 is a square wave which is on for $0.5\,s$ and then off for $0.5\,s$.

Figures 5.6 through 5.9 show a comparison of four different open-loop step responses between the experiment, linear system, and the nonlinear model. The nonlinear model shows a better prediction of the steady-state gains since it is able to interpolate from the experimental data. An overall comparison of the dynamic response of the systems show that the linear model and the nonlinear model are nearly identical as might be expected.

6. Results. Based on the PID discrete control design, it was predicted that using only integral control would best meet the design objectives for the feedback controller. The linear simulations using the integral controller in Fig. 4.8, showed the closed-loop response for $K_I = 5, 6,$ and 7. Setting the integral gain $K_I = 6.946$, the feedback controller was then implemented on the experimental closed-loop system. The results from this experimental data are shown in Fig. 6.1. The test was performed by setting the value of $P_i - P_s = 10$ and then turning on the controller at $t = 0$ given a desired pressure recovery parameter, $dC_P/dx_{des} = 1.9$. The experimental data shows that the controller performed

well and had very little overshoot and a good response time. Figure 6.1 also shows the predicted response of the linear and nonlinear models. Both models were able to predict the experimental closed-loop response relatively well and the transient response for dC_P/dx was predicted very well by the linear model. The prediction by the nonlinear model for the dC_P/dx transient was good, but had a slightly larger overshoot than the experimental results. Both the linear and nonlinear models showed larger oscillation in the cavity pressure fluctuations p'/ρ_∞ and inlet pressure $P_i - P_s$ as compared to the experimental data. Figure 6.2 shows a comparison between the open-loop response and closed-loop response for the experimental system. The open-loop response was performed by using a step input in $P_i - P_s$ using the initial and final values given by the closed-loop simulation. This figure shows that dC_P/dx and p'/ρ_∞ for the open-loop response, has a faster response time but at the cost of a larger overshoot. This figure also shows that there is a slow transient in the flow system. At $t = 25\,s$, dC_P/dx has reached its desired value of 1.9, yet the cavity pressure fluctuations are still being increased by the integral controller. On the other hand, the open-loop step input shows that dC_P/dx is slightly higher than the desired value at $t = 25\,s$ and then slowly drifts to the desired value. This shows the advantage of the feedback controller since it is able to hold the desired pressure gradient while the flow system goes through a slow transient.

Using the same integral gain, the controller was tested using a step down in the desired dC_P/dx command. In this regime the steady-state gains start to deviate from the linear model fit as shown in Fig. 3.4. Figure 6.3 shows the closed-loop experimental data where the initial inlet pressure was set to, $P_i - P_s = 20$ and the controller was turned on at $t = 0$ with $dC_P/dx = 1.64$. The response of the closed-loop system displayed large oscillations in the dC_P/dx signal, which settled down near $t = 50\,s$. The nonlinear model also shows large oscillations which did not settle down where the linear model had mild oscillations for the closed-loop simulation. Neither model was able to predict the closed-loop response in this regime but they did predict the unsteady behavior for $K_I = 6.946$. The linear model is certainly not valid in this regime since it does not account for the steady-state gain shown in Figs. 3.3 and 3.4. The nonlinear model does include the nonlinear steady-state gain but is still unable to accurately model the closed-loop system. To improve the nonlinear model in this regime, more steady-state and dynamic data is needed.

By reducing the integral gain, the closed-loop response in the nonlinear regime can be improved. Figure 6.4 shows the closed-loop experimental data for $K_I = 4.63$ along with the linear and nonlinear simulations. The dC_P/dx transient has improved but there are still some mild oscillations in the experimental closed-loop system. The nonlinear model still predicts a continuing oscillation for this gain and the linear model is able to capture the average transient response but does not capture the oscillations seen in the experimental data. Reducing the integral gain to $K_I = 2.315$, the transient response is much smoother at the cost of a slower response time as shown in Fig. 6.5. Both the linear and nonlinear models show good agreement with the experimental data. Figure 6.6 shows a comparison between the closed-loop and open-loop step input responses. This comparison shows how the open-loop response has a large overshoot in the cavity pressure fluctuations and some oscillations in the value of dC_P/dx. The integral controller shows how it increases the damping effect of the transient response by shaping the input command $P_i - P_s$. This smoother inlet pressure command does not excite the higher frequency dynamics of the system like the open-loop step input. Figure 6.7 shows the effect of decreasing the integral gain for the experimental closed-loop system. This comparison shows how a smaller integral gain of $K_I = 2.315$ minimizes the overshoot and oscillations produced by the controller.

7. Conclusions. This investigation demonstrated the incorporation of digital feedback control into an open-loop flow control experiment. The objective of the feedback controller is to track a desired pressure gradient measured in the controlled flow region. This pressure gradient characterizes the degree of flow separation (or attachment) and hence the lift, drag, and moment forces acting on the generic hump model. The oscillatory excitation, which controlled the flow in the separated region, operated at $385\,Hz$. The degree of flow separation was then controlled by changing

the magnitude of the oscillatory excitation. The actuator system which changed the magnitude of the oscillatory excitation, had a frequency response of $0.05 Hz$, which is much slower than the flow response. Therefore from the flow physics point of view, the changes in the magnitude of the oscillatory excitation are performed in a quasi-steady manor. The dynamics of the open-loop system are then the dynamics of the actuator system and do not include dynamics of the controlled flow region. Experimental data from open-loop step inputs showed that the actuator system could be modeled by a simple second-order model.

A PID control design approach was used since it could be tuned to give good performance results where only the dominant system time constants are known. The PID control design showed that using only integral gain was the most effective as a result of the large time constant of the actuator system. The control design showed that adding a proportional or derivative gain would only amplify the oscillations produced by the small fluctuations in the wind tunnel test conditions. The closed-loop experiments demonstrated that the integral feedback controller was able to improve the transient response of the open-loop system by minimizing the overshoot seen in the open-loop experiments. Overall, the integral controller did a good job in tracking the desired pressure gradient in the controlled flow region. It should be noted that while the PID control design was reasonably simple, the application of a digital feedback controller to a flow control experiment is unique. This closed-loop experiment is the first in a series of experiments which will incorporate digital feedback control to existing NASA Langley flow control experiments. The knowledge and insights gained from this experiment will be valuable for future closed-loop flow control experiments.

REFERENCES

[1] *SIMULINK, a dynamic system simulator for MATLAB, MATLAB reference guide*. The Math Works, Inc., 1999.

[2] G. F. FRANKLIN, J. D. POWEL, AND A. EMAMI-NAEINI, *Feedback Control of Dynamic Systems*, Addison-Wesley, New York, 1994.

[3] R. ISERMANN, *Digital Control Systems, Volume I*, Springer-Verlag, New York, 1989.

[4] A. C. LADSON AND J. E. RAY, *Evolution calibration, and operation characteristics of the two-dimensional test section of the Langley 0.3-meter transonic cryogenic wind tunnel*, Tech. Report TP-2749, NASA Langley Research Center, Hampton, VA 23681-2199, 1987.

[5] A. R. RALLO, A. D. DRESS, AND A. J. H. SIEGLE, *Operating envelope charts for the Langley 0.3-meter transonic cryogenic wind tunnel*, Tech. Report TM-89008, NASA Langley Research Center, Hampton, VA 23681-2199, 1986.

[6] A. SEIFERT, T. BACHAR, D. KOSS, M. SHEPSHELOVICH, AND I. WYGNANSKI, *Oscillatory blowing, a tool to delay boundary layer separation*, AIAA Journal, 31 (1993), pp. 2052–2060.

[7] A. SEIFERT, A. DARABI, AND I. WYGNANSKI, *On the delay of airfoil stall by periodic excitation*, AIAA Journal of Aircraft, 33 (1996), pp. 691–699.

[8] A. SEIFERT AND L. G. PACK, *Active control of separated flows on generic configurations at high Reynolds numbers*. AIAA 99-3403, 1999.

[9] A. SEIFERT AND L. G. PACK, *Oscillatory control of separation at high Reynolds numbers*, AIAA Journal, 37 (1999), pp. 1062–1071.

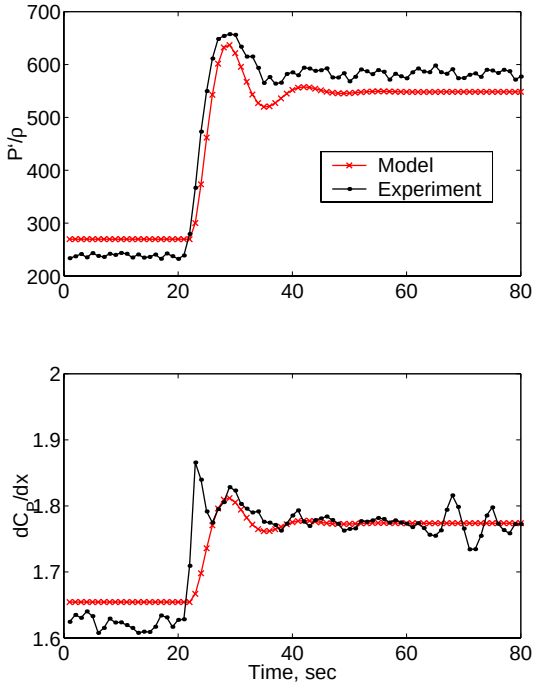

FIG. 3.6. *A comparison of an open-loop step input of* $P_i - P_s$ *from* 10 *to* 15 *for the experimental system and the linear discrete model*

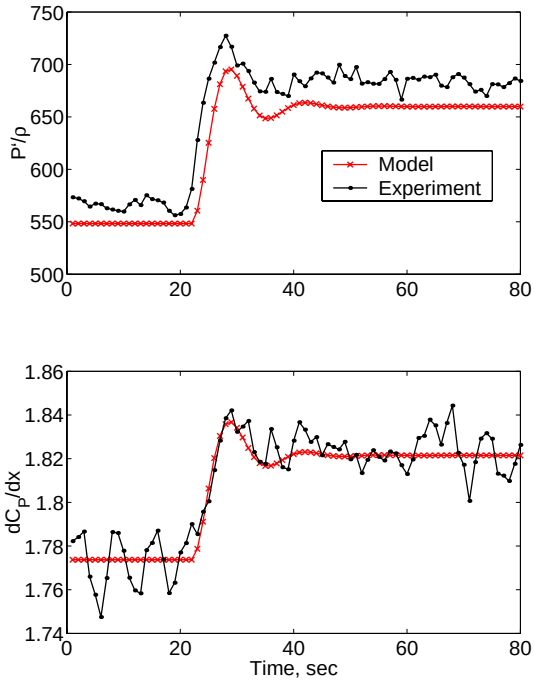

FIG. 3.7. *A comparison of an open-loop step input of* $P_i - P_s$ *from* 15 *to* 17 *for the experimental system and the linear discrete model*

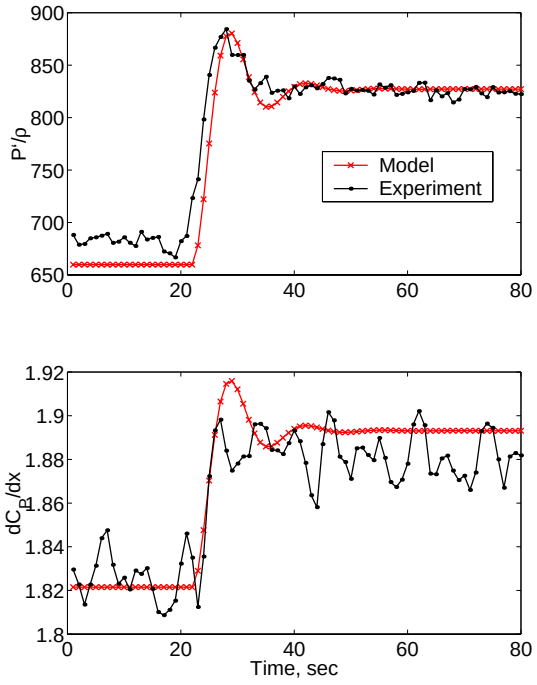

FIG. 3.8. *A comparison of an open-loop step input of* $P_i - P_s$ *from* 17 *to* 20 *for the experimental system and the linear discrete model*

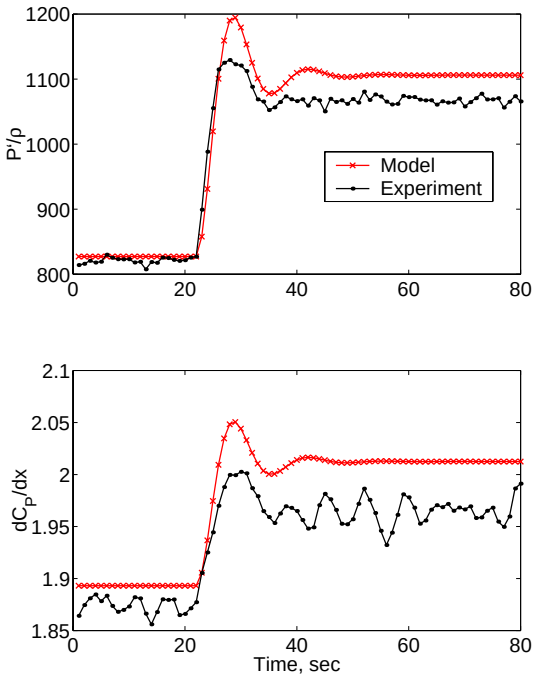

FIG. 3.9. *A comparison of an open-loop step input of* $P_i - P_s$ *from* 20 *to* 25 *for the experimental system and the linear discrete model*

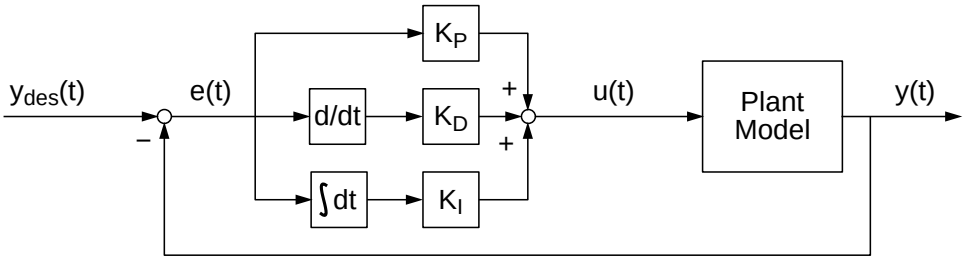

FIG. 4.1. *Block diagram for PID controller.*

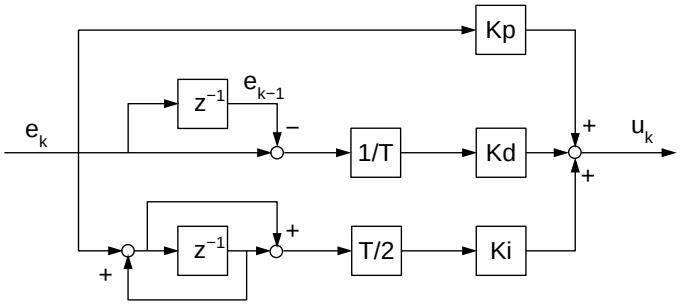

FIG. 4.2. *Block diagram for digital PID controller.*

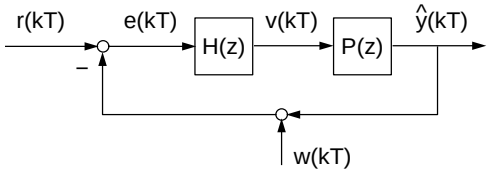

FIG. 4.3. *Block diagram of the closed-loop system.*

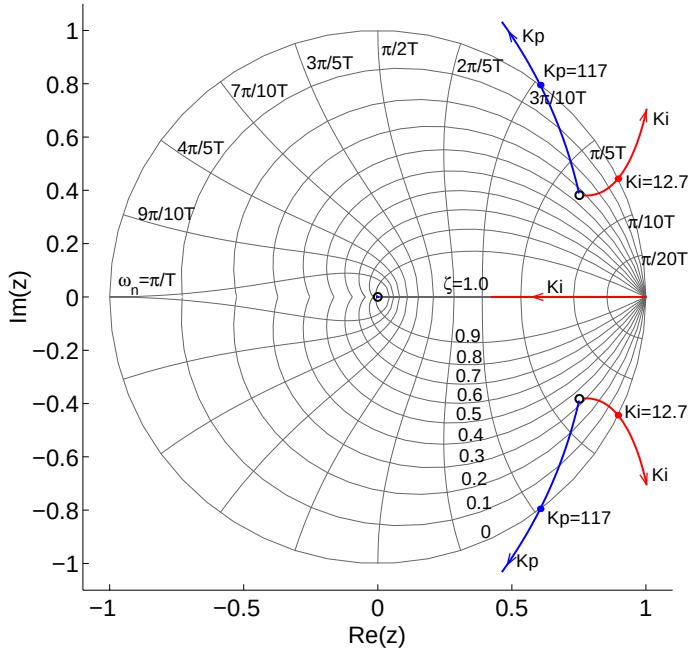

FIG. 4.4. *Root locus of closed-loop system in the z-plane using proportional and integral feedback gain. The K_P lines show how the open-loop poles (circles) move using only proportional feedback. Similarly the K_I lines show how the open-loop poles move when using only integral feedback.*

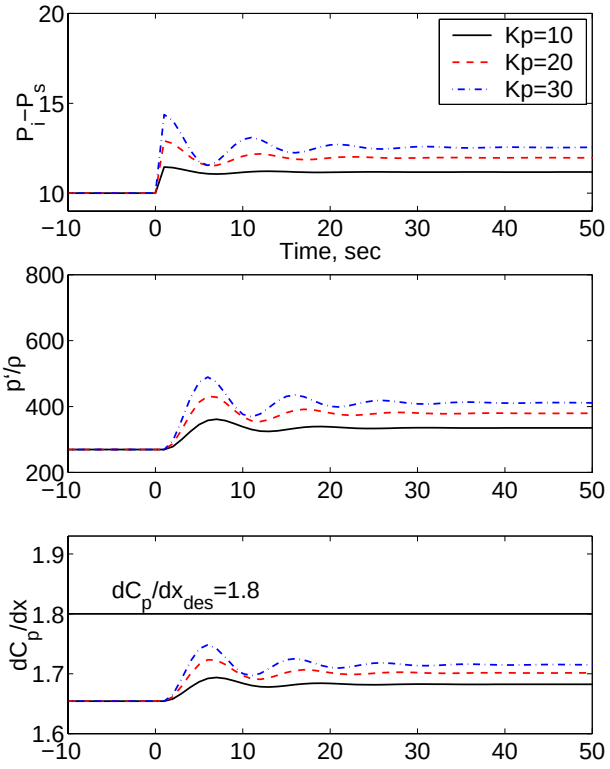

FIG. 4.5. *Closed-loop simulation using the linear state model for feedback gains $K_P = 10, 20, 30$ where $K_I = K_D = 0$.*

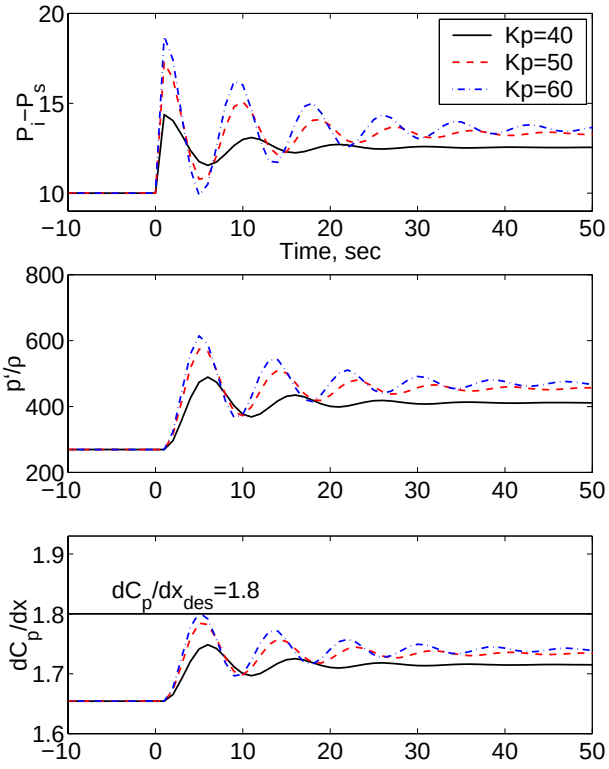

FIG. 4.6. *Closed-loop simulation using the linear state model for feedback gains $K_P = 40, 50, 60$ where $K_I = K_D = 0$.*

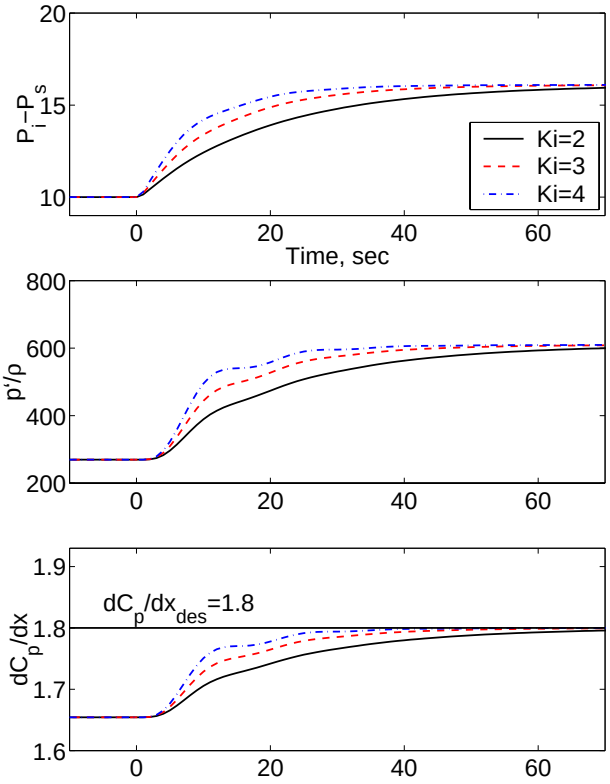

FIG. 4.7. *Closed-loop simulation using the linear state model for feedback gains $K_I = 2,3,4$ where $K_P = K_D = 0$.*

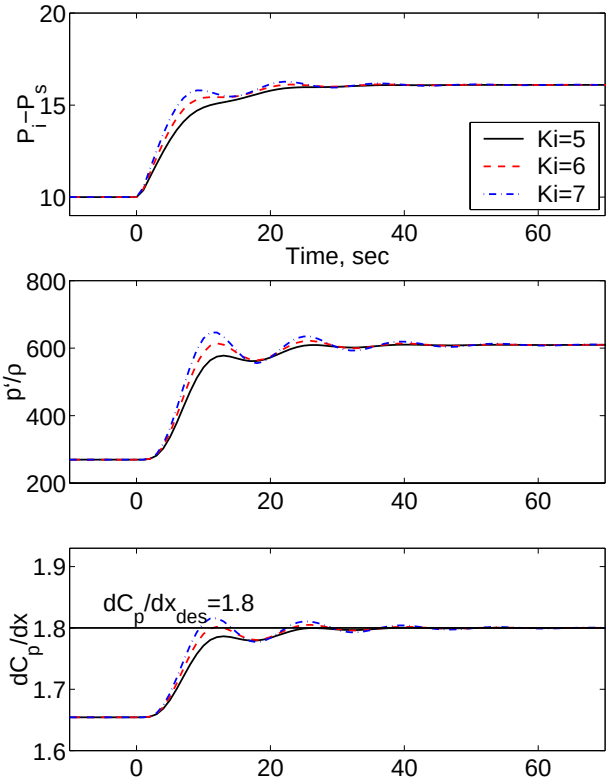

FIG. 4.8. *Closed-loop simulation using the linear state model for feedback gains $K_I = 5,6,7$ where $K_P = K_D = 0$.*

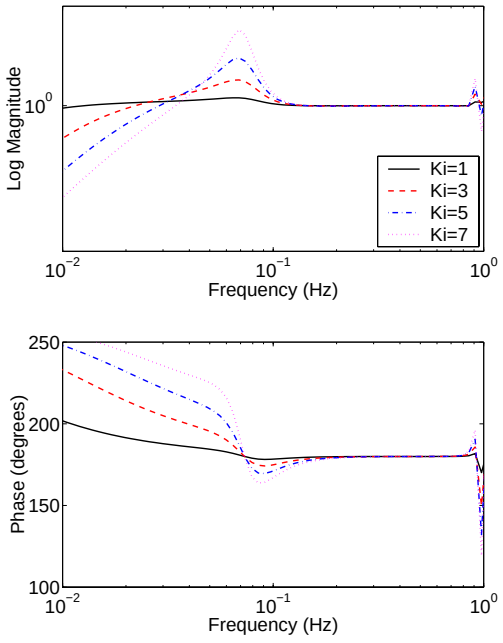

FIG. 4.9. *Bode plot of closed-loop transfer function from the noise input w to the error e, for increasing values of K_I.*

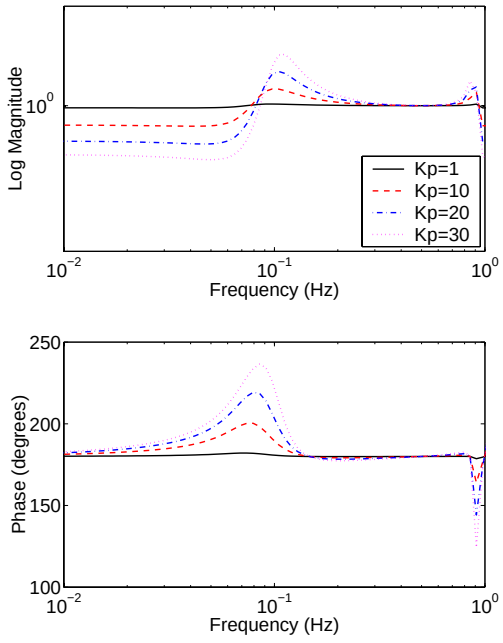

FIG. 4.10. *Bode plot of closed-loop transfer function from the noise input w to the error e, for increasing values of K_P.*

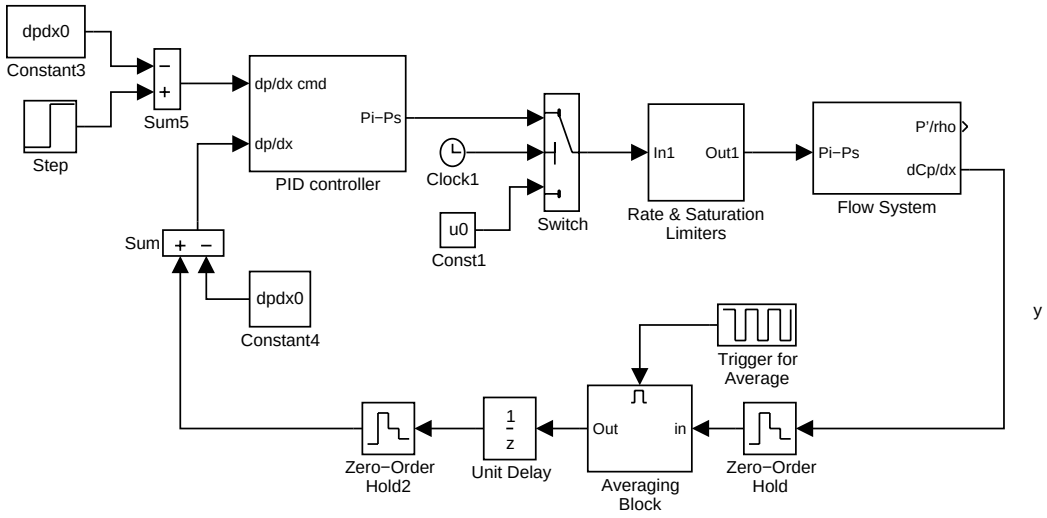

FIG. 5.1. *Block diagram of the closed-loop system.*

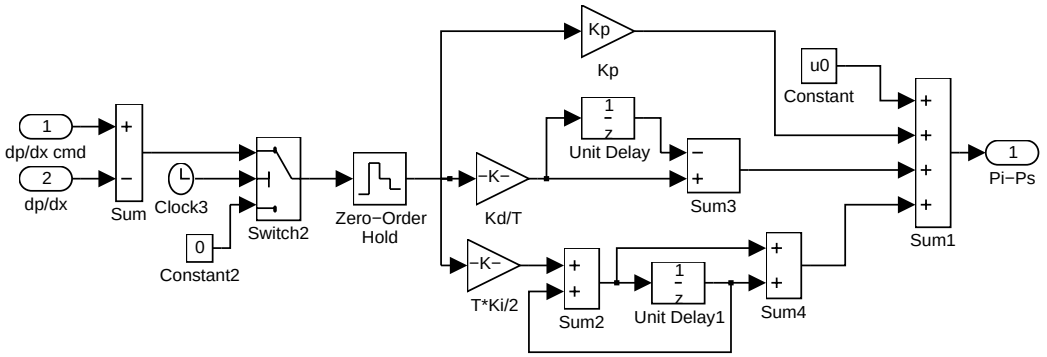

FIG. 5.2. *Block diagram of the PID controller.*

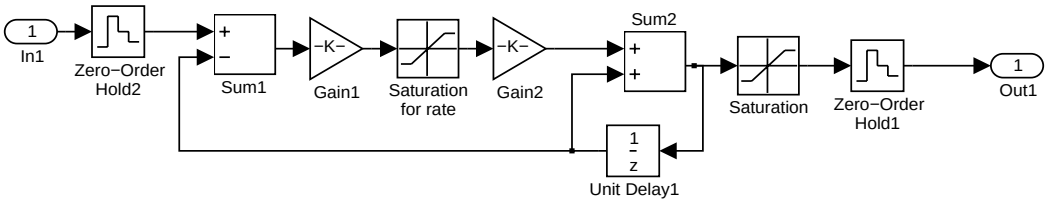

FIG. 5.3. *Block diagram of the rate and saturation limiters.*

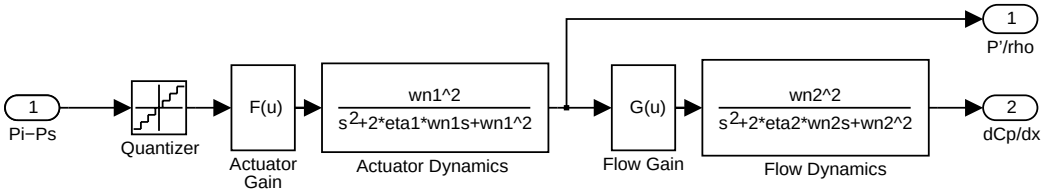

FIG. 5.4. *Block diagram of the flow system model.*

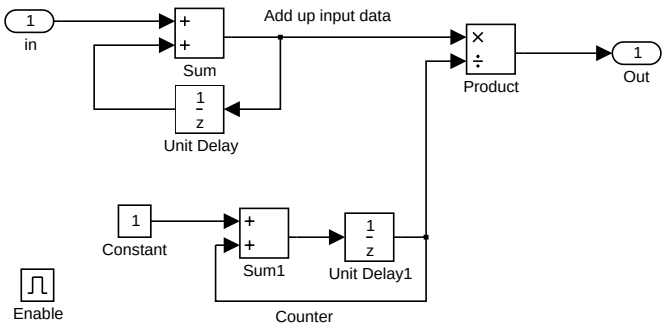

FIG. 5.5. *Block diagram of the averaging block.*

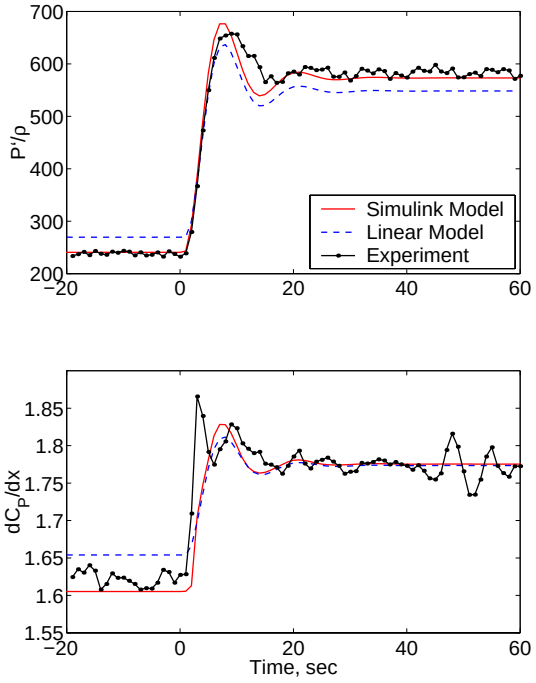

FIG. 5.6. *A comparison of an open-loop step input of* $P_i - P_s$ *from* 10 *to* 15 *for the experimental system, the linear discrete model, and the nonlinear model*

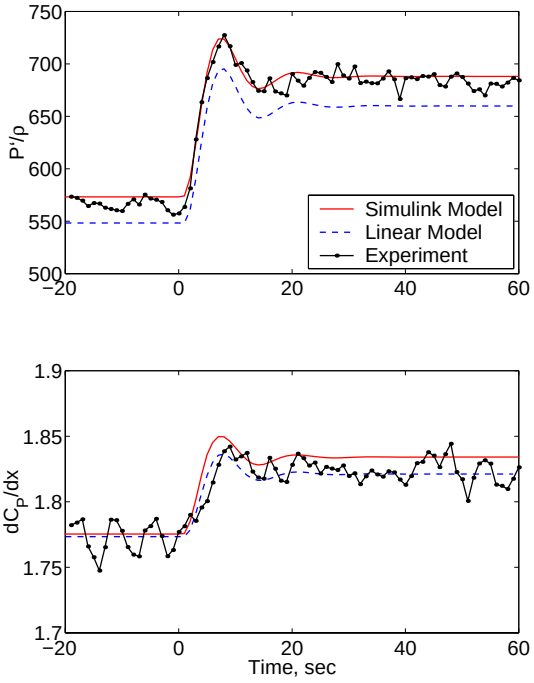

FIG. 5.7. *A comparison of an open-loop step input of* $P_i - P_s$ *from* 15 *to* 17 *for the experimental system, the linear discrete model, and the nonlinear model*

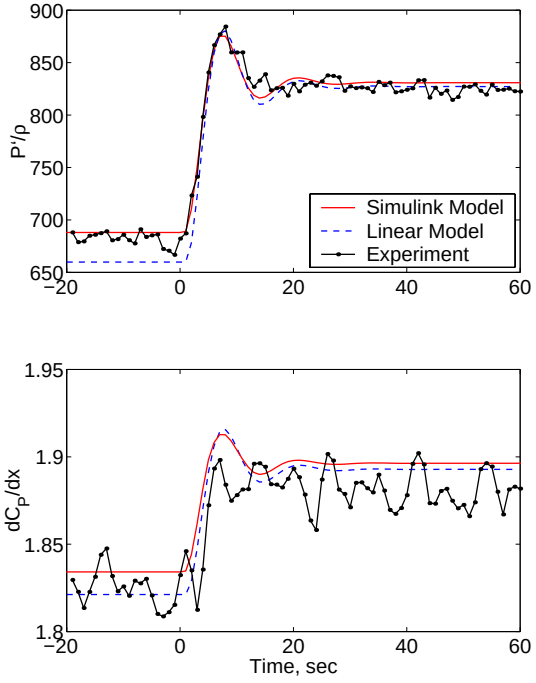

FIG. 5.8. *A comparison of an open-loop step input of* $P_i - P_s$ *from* 17 *to* 20 *for the experimental system, the linear discrete model, and the nonlinear model*

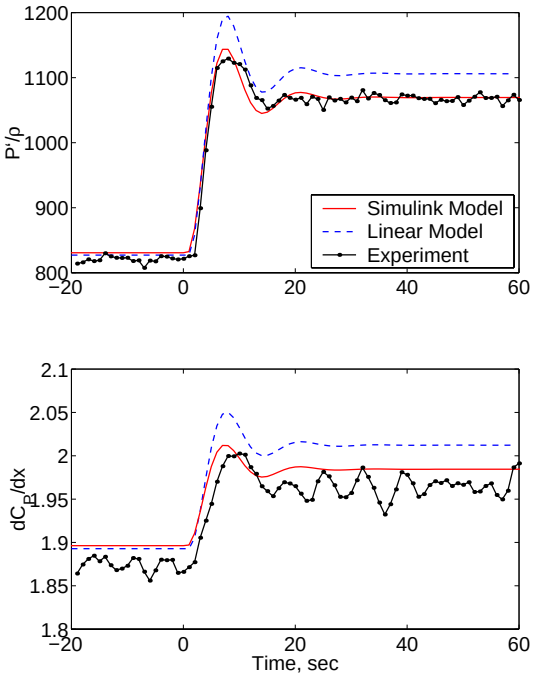

FIG. 5.9. *A comparison of an open-loop step input of* $P_i - P_s$ *from* 20 *to* 25 *for the experimental system, the linear discrete model, and the nonlinear model*

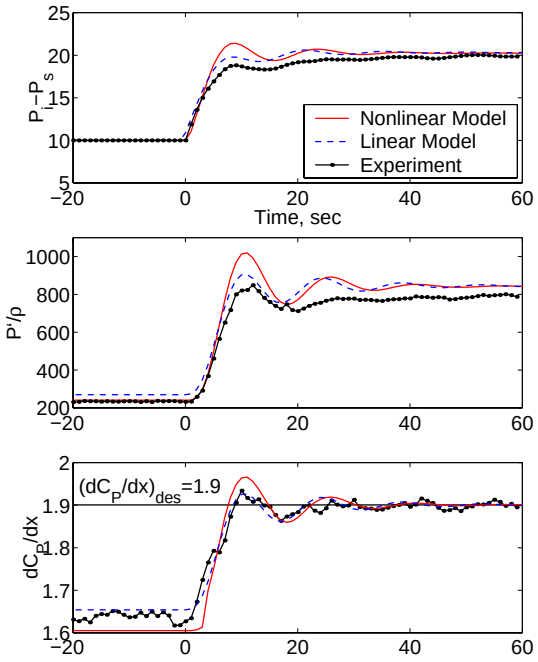

FIG. 6.1. *Closed-loop response of the nonlinear model and the experimental system for* $(dC_P/dx)_{des} = 1.9$ *where the controller was turned on at* $t = 0$*. The PID controller had the gains,* $K_P = 0, K_I = 6.946$*, and* $K_D = 0$*.*

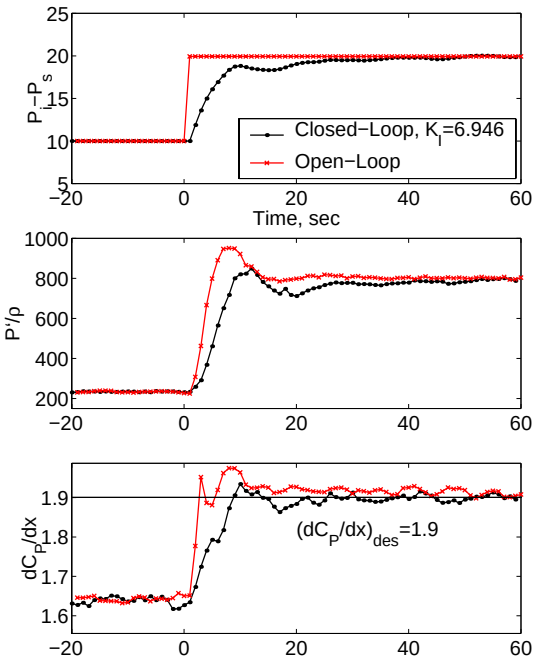

FIG. 6.2. *A comparison of the open-loop step input response to the closed-loop system using* $K_I = 6.946$*.*

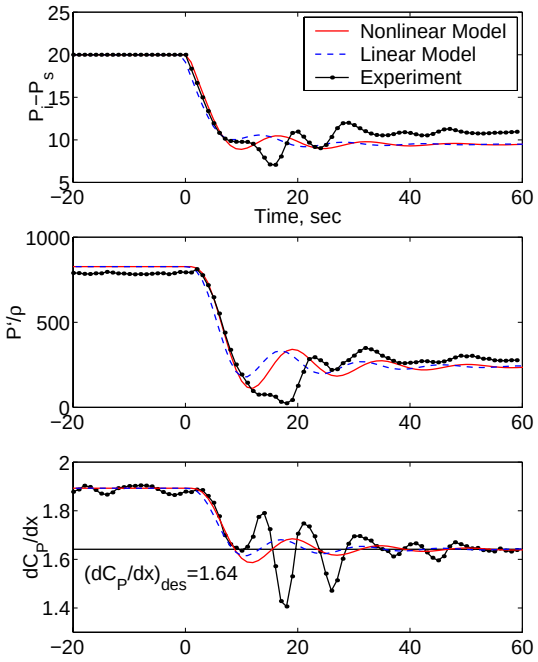

FIG. 6.3. *Closed-loop response of the nonlinear model and the experimental system for* $(dC_P/dx)_{des} = 1.64$ *where the controller was turned on at* $t = 0$*. The PID controller had the gains,* $K_P = 0, K_I = 6.946$*, and* $K_D = 0$*.*

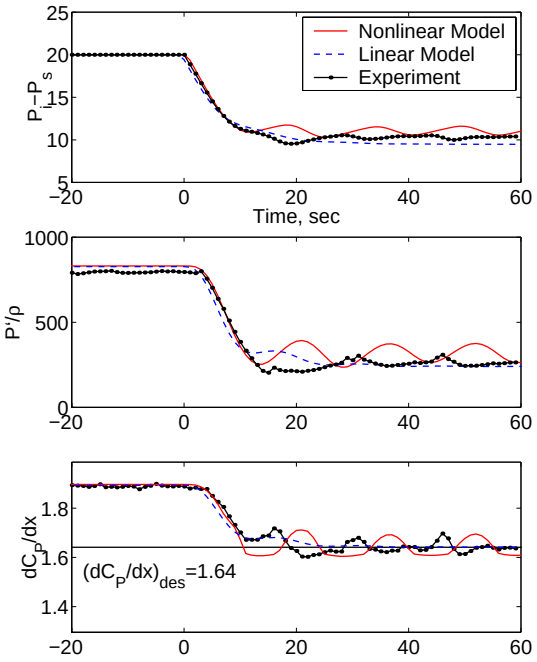

FIG. 6.4. *Closed-loop response of the nonlinear model and the experimental system for* $(dC_P/dx)_{des} = 1.9$ *where the controller was turned on at* $t = 0$*. The PID controller had the gains,* $K_P = 0, K_I = 4.64$*, and* $K_D = 0$*.*

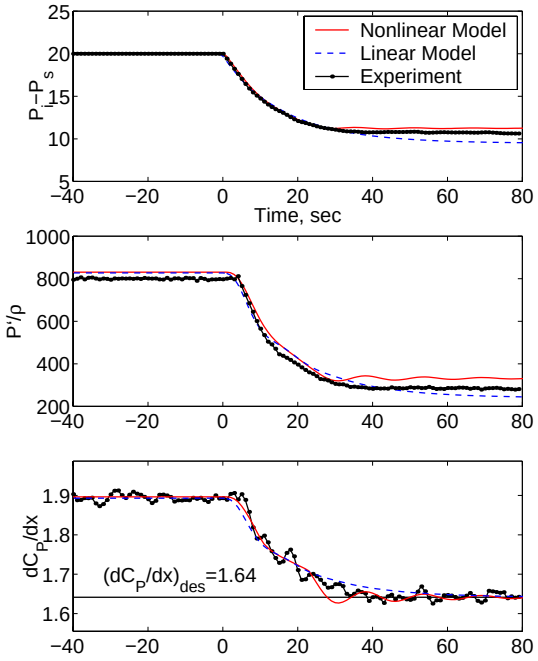

FIG. 6.5. *Closed-loop response of the nonlinear model and the experimental system for* $(dC_P/dx)_{des} = 1.9$ *where the controller was turned on at* $t = 0$. *The PID controller had the gains,* $K_P = 0, K_I = 2.315$, *and* $K_D = 0$.

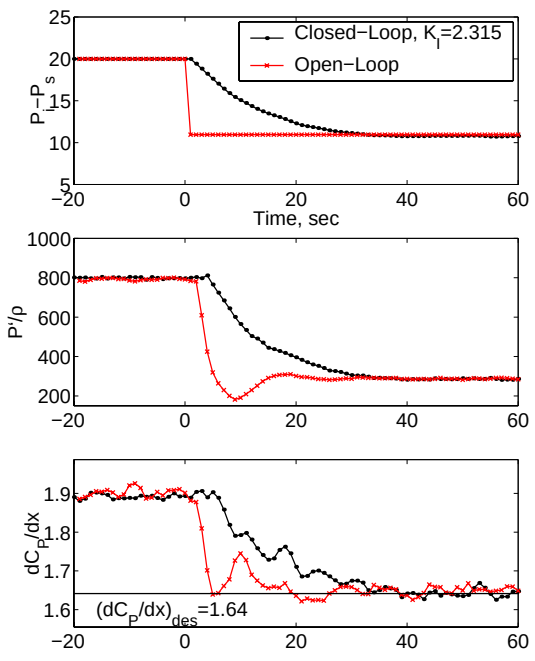

FIG. 6.6. *A comparison of the open-loop step input response to the closed-loop system using* $K_I = 2.315$.

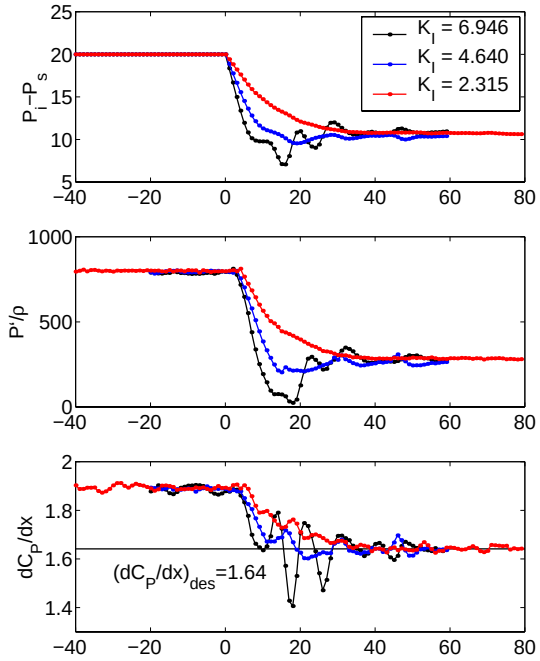

FIG. 6.7. *A comparison of the experimental closed-loop transient responses for three* K_I *values.*